International Journal of Engineering

Journal Homepage: www.ije.ir

Development of Temperature-strain Prediction Based on Deformation-induced Heating Mechanism in SCM440 Surface Cracked Shaft under Ultrasonic Excitation

P. Lap-Arparat, K. Tuchinda*

Material Manufacturing and Surface Engineering Research Center (MaSE), The Sirindhron International Thai-German Graduate School of Engineering (TGGS), King Mongkut's University of Technology North Bangkok (KMUTNB), Bangkok, Thailand

P A P E R I N F O

Paper history:
Received 13 August 2023
Received in revised form 07 September 2023
Accepted 09 September 2023

Keywords:
Cracked Shaft
Deformation-induced Heating
Elliptic Crack Parameter
SCM440
Temperature-Strain Analysis
Vibrothermography Inspection Method

A B S T R A C T

The mechanisms behind temperature and material deformation in vibrothermography remain questionable, presenting a gap in understanding. This study investigates the deformation-induced mechanism, focusing solely on the heat generation associated with strain development. Both experimental and simulation approaches are incorporated. The experimental segment explores the temperature-strain relationship of SCM440 material, commonly used for rotating shafts. This behavior is examined through the connection between temperature change and material deformation during a uniaxial tensile test. Results indicate that temperature change and distribution can be predicted based on plastic strain development. Finite Element Method (FEM) simulation is utilized to model the excitation of a shaft with and without an elliptic surface crack. Various cracked shaft configurations are investigated, revealing distinct strain generation and distribution patterns. High strain alteration is notably observed around the crack tips, enabling the detection of shaft discontinuity. Consequently, a temperature prediction technique is developed to estimate temperature based on strain alteration during deformation. Adequate excitation power and the use of a high-sensitivity IR camera are recommended for the effective application of the temperature prediction technique. Additionally, this study provides insights into understanding the utility and limitations of vibrothermography for inspecting engineering component damage based on experimental temperature-strain relationships and computational predictions of strain distribution in cracked shafts under excitation. These findings offer guidance for engineering applications and future research endeavors.

***doi**: 10.5829/ije.2024.37.01a.14*

Graphical Abstract

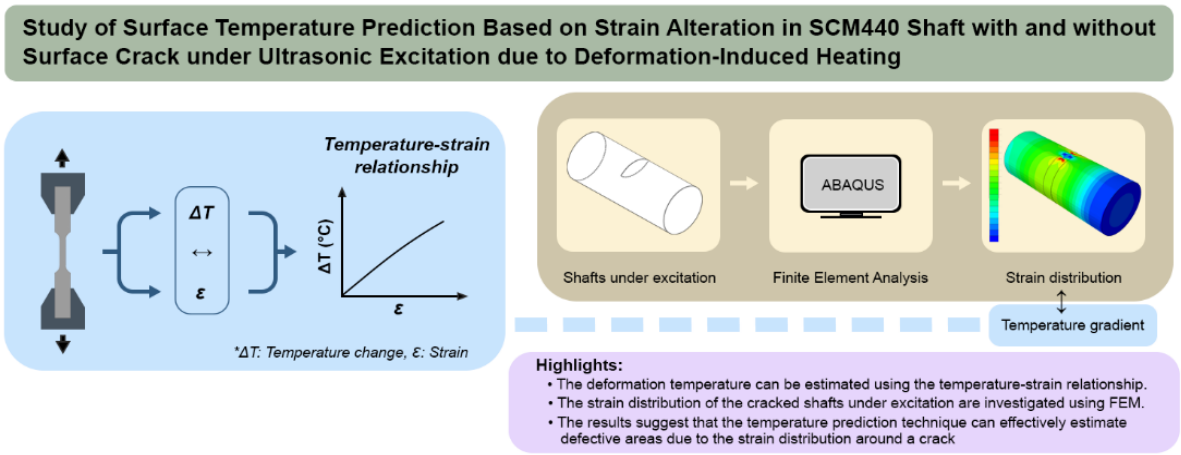

*Corresponding Author Email: karuna.t@tggs.kmutnb.ac.th (K. Tuchinda)

Please cite this article as: Fereshteh-Saniee N, Elmkhah H, Molaei M, Zolriasatein A. Development of Temperature-strain Prediction Based on Deformation-induced Heating Mechanism in SCM440 Surface Cracked Shaft under Ultrasonic Excitation. International Journal of Engineering, Transactions A: Basics, 2024;37(01):151-166.

1. INTRODUCTION

Vibrothermography (VT) is a technique to investigate the defect located on either the surface or near the surface via thermal energy release (1). This inspection technique requires an infrared (IR) camera to detect the diffused heat from vibrated defects. When the defects are vibrated, they rapidly generate heat that is diffused and radiated outward to the surface, which can be observed in a short time (2). Therefore, VT is less consumed in the inspection time compared with another nondestructive testing (NDT) technique, which is requisite for industrial interests. VT was first introduced in the late 80s by Reifsnider et al. (3). A series of experiments were conducted with noticeable heat generation in materials, and the thermographic pattern of heating depended on the material properties and structural geometry referred to by Reifsnider et al. (3) These indicated the unique characteristics of the thermal energy release on a specific material. Subsequently, VT became well-known after Favro et al. (4) placed an ultrasonic welder with a maximum power of 1 kW for the excitation source. Thereafter, an IR camera revealed the glow of a crack immediately after a sonic pulse was applied, which influenced more availability and reliability for industrial applications.

According to the industrial components, the metallic cylindrical-shaped component is a common part frequently involved in any system of the industry, i.e., axle, pin, shaft, etc. (5) Defects in these components are generally discovered as fatigue cracks, especially during the observation of shafts (6). In general, fatigue cracks are inevitable and normally appear in components that have operated repeatedly (7). A fatigue crack on a shaft can be initiated from a small discontinuity that occurs on the surface and transversely propagates to the center under cyclic loading conditions, which sequentially directs a large discontinuity and complete fracture (8-10). Recently, it has been observed that VT was applied for inspecting defects in industrial components, i.e. turbine disks, gas turbine blades, welded parts, etc. (11-14). The results revealed the good detectability of this inspection; VT could detect a known fatigue crack of 0.015 mm in length with a better possibility of detection (POD) than the traditional method (15). In addition, VT was capably performed on various materials such as concrete (16, 17), ceramics (18), polymers (19, 20), and metals (21-23). The aforementioned studies confirmed the usability, rapidity, and variety of this inspection method.

Vibroacoustic thermography (VT), also known as sonic IR and thermosonics, currently relies mainly on IR cameras and ultrasonic excitation. Ultrasonic excitation is typically selected at a predetermined frequency of 20, 40, or 60 kHz (24). However, the heating mechanism of VT remains questionable as it is not fully understood (14). It has been found that researchers attempted to investigate the source of heat generation. There are 2 major sources that have been discussed: (1) Frictional rubbing and (2) Deformation-induced heating (25). For instance, the severity of the closure crack rubbing during vibration can cause heat generation due to friction between the contracting faces of the crack. The evidence of frictional heating is shown in the following literature (26-28). Besides the closure crack, the asperity might be included, meaning no rubbing between crack faces. The heat can be induced beyond the crack tip due to the structural deformation under the vibration causing the stress concentration in the plastic zone, which is also known as plasticity-induced heating (29, 30). Nonetheless, deformation-induced heating in metal is rarely divulged due to the absence of demonstration. Therefore, the study of deformation-induced heating in metallic material is necessary for a better understanding of these heating mechanisms.

The understanding of material characteristics expedites the ability to estimate limitations or potential damage to engineering components within the system. In several instances, material characteristics have been employed to simulate their behavior under real working conditions or relevant scenarios in analytical models. The behavior of structures exhibits responses under assigned loading conditions, which aids in investigating structural deformations such as damage, elasticity, plasticity, and vibration (31-33). Analyzing these responses indicates the structural component usage experienced during operational conditions, allowing for the prediction of fatigue and service life (34-37). A similar approach is adopted to investigate temperature changes resulting from deformation-induced heating in this study. The developed temperature prediction technique demonstrates the object's temperature based on the corresponding strain alteration during deformation. This study aims to establish a fundamental understanding of the deformation-induced heating mechanism and to enhance the comprehension of the VT inspection technique used in engineering components excluding the frictional heating from closure cracks, serving as a foundation for future developments in industrial applications.

In this study, the temperature prediction technique was examined based on deformation-induced heating from the perspective of the vibrothermography inspection method. The study focused on the inspection of engineering parts that are widely used in industrial systems. The circular SCM440 shaft was selected for the study as it is commonly used for shafts in many applications (38). The study included both experimental and computational research. The experimental-based research was performed on the investigation of the temperature-strain relationship of the selected material for developing the prediction technique. Meanwhile, the computational research observed the response of the

shaft under virtual ultrasonic excitation to investigate the influence of the controlling parameters including crack shape, crack size, and excitation conditions. This study attempted to determine the strain characteristics of the shafts, either with a crack or without a crack. The developed temperature prediction technique was applied afterward to estimate the temperature of the shaft based on the computed strain under ultrasonic excitation. The research methodology flowchart is illustrated in Figure 1.

2. EXPERIMENTAL INVESTIGATION OF THE TEMPERATURE-STRAIN RELATIONSHIP ON SCM440 MATERIAL

As reported by Reifsnider et al. (3), thermal characteristics are individually dependent on the material. To understand the behavior of temperature induced during structural deformation based on deformation-induced heating, the thermal characteristics of SCM440 (AISI 4140) due to structural deformation were investigated. From observation of previous experimental work conducted by Kapoor and Nemat-Nasser (39), the temperature (T) of an object during deformation can be described as Equation 1:

$$T = T_0 + \Delta T \quad (1)$$

where T_0 is an initial temperature and ΔT is the temperature change due to the deformation. In this work, the temperature change (ΔT) was investigated via the experiment with the following details.

2. 1. Material Properties and Experimental Preparation SCM440 steel was machined into flat tensile specimens according to ASTM E8 standard for uniaxial tensile testing and chemical composition, as shown in Table 1. The inspection points on the specimen were selected to be in the gauge length and were marked as P1, P2, and P3. The P2 was in the middle of the specimen, while P1 and P3 were marked away from P2 with an equal spacing of 6 mm (see Figure 2). The influence of the surface preparation on the temperature-strain relationship was included in this investigation. During the surface preparation process, the specimens were ground in different directions, denoted as the axial direction (Y-axis) and transverse direction (X-axis), as illustrated in Figure 2. Furthermore, the Pulstec μ-X360s was applied for X-Ray Diffraction (XRD) analysis. The cosine technique was performed with an incident angle of 35° to investigate the residual stress at marked locations. Lastly, the specimens were sprayed in a sparkle pattern to be ready for strain analysis using the GOM Digital Image Correlation (DIC) system.

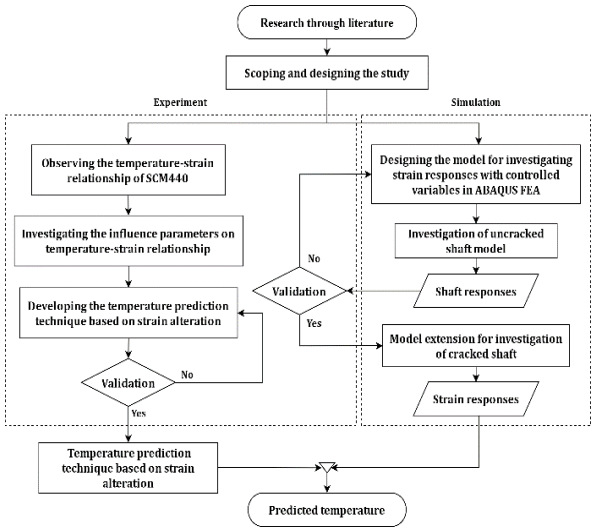

Figure 1. Research methodology flowchart

2. 2. Procedure A prepared specimen was attached with K-type thermocouples to the marked location and mounted on the universal testing machine. The thermocouples were connected to the NI-9213 temperature module for data logging. The sensitivity of the temperature-measuring module with K-type thermocouples was 0.02°C in resolution mode. An

TABLE 1. Chemical composition of SCM440 material

Element	C	Si	Mn	P	S	Cr	Cu	Ni	Mo
%Weight	0.41	0.23	0.78	0.16	0.13	1.06	0.02	0.01	0.17

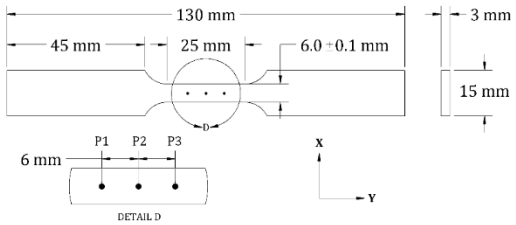

Figure 2. Dimensions of ASTM E8 specimen with marked point

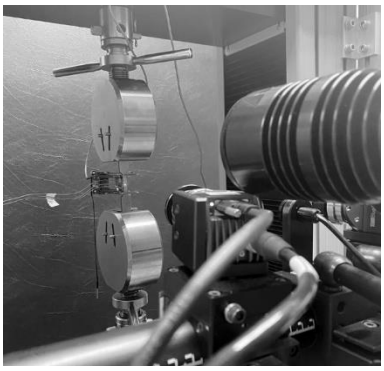

Figure 3. Experimental setup

extensometer and GOM ARAMIS adjustable camera were used for strain measurement where an extensometer griped across the specimen gauge and a GOM camera captured a deformation on the surface of the specimen, as shown in Figure 3. The tests were conducted at room temperature with 0.5 mm/min testing speed. A sampling rate was set at 1 Hz for all data logging. In the post-process step, GOM Correlate software was applied to analyze the local strain at the location of the thermocouple attachment that constructed the temperature-strain relationship.

This temperature-strain relationship exposed the temperature of the SCM440 object via strain alteration. Comprehension of the temperature-strain relationship was utilized to explain the behavior of the cracked shaft on the strain response under excitation, which was investigated in the computational study.

3. COMPUTATIONAL STUDY OF SURFACE CRACKED AND UNCRACKED SHAFT ON STRAIN RESPONSE UNDER EXCITATION

In this session, VT was applied to a shaft, which is a common part of the rotating machinery in industry. Surface cracked and uncracked shafts were subjected to excitation using a low-power ultrasonic cleaning transducer. The application of a low-power ultrasonic cleaning transducer as an excitation source for VT has been previously published (40-42). Cracks can propagate when applied force exceeds the resistance of the material, resulting in the release of stored energy (43). Before crack propagation, the quasistatic energy was stored in a small region beyond the crack tip, known as the plastic zone. Considering the early stage of loading, the fracture-characterizing parameter, i.e., the stress intensity factor (K), was used to define the stress fields. An example of the stress fields for the opening mode (Mode I) can be determined by Equation 2 (44):

$$\sigma^{(I)} = \frac{K_I}{\sqrt{2\pi r}} f^{(I)}(\theta) \quad (2)$$

where r denotes the distance from the tip and $f(\theta)$ is the angular function that depends on the crack geometry and fracture mode; the mode of fracture was also based on the loading condition (43). From Equation 2, crack geometry and the condition of load governed the behavior of the stress fields near the tip.

The stress and strain relationship could be described by the material model. For metal and alloy, the strain (ε) is usually directly proportional to stress (σ) under elastic deformation, which obeys Hooke's law and could be expressed as Equation 3:

$$\varepsilon = \frac{\sigma}{E} \quad (3)$$

where E was the elastic modulus of the material.

The elastic strain around the crack tip is related to the loading condition and crack geometry. The effect of loading conditions and crack geometry were considered and investigated in this study. The finite element method (FEM) is a preferred method used for such analysis in the field of fracture mechanics. Several studies have utilized FEM to analyze the elastic-plastic response in various ways (45-50). In this study, ABAQUS FEA software was employed for the investigation of influences of crack geometry and loading conditions on the strain responses of both surface cracked and uncracked shafts.

3. 1. Computational Model This study aimed to investigate the strain response of a shaft under excitation using a low-power ultrasonic cleaning transducer. The initial step involved experimental calibration of the 40 kHz ultrasonic cleaning transducer in the laboratory. A 100 W signal generator was used to determine the force exerted during the transducer's operation, resulting in a force of 0.35 N. This force was applied as the excitation load (P) in the subsequent computational model. The computational model was created in ABAQUS FEA and represented a 3D cylindrical shape resembling both cracked and uncracked shafts. The dimensions of the shaft were derived from a drive shaft in a water pump system with measurements of 24 mm in diameter and 60 mm in length. The material chosen for the shaft was SCM440, a commonly used material for shaft applications. The stress-strain behavior of SCM440 was obtained through uniaxial tensile testing in the laboratory. The computational model employed implicit-dynamic analysis to study the transient strain alteration under excitation. Note that, this study illustrated the methodology particularly on the adopted shaft geometry. The purposed methodology could later be extended without major difficulty to investigate other components with different geometry.

A simple cylindrical model was used to represent the uncracked shaft. For the cracked shaft, the contour integral technique, which is favored for studying the effect around the crack tip, was applied to create the crack. The elastic-plastic, power-law hardening material was adopted to control the strain singularity at the crack tips, which is commonly used for a stress-strain field analysis near the tips of elastoplastic materials (51-54). The cracks contained a crack front and crack faces, as illustrated in Figure 4. The crack tip that was located close to the angular displacement (θ) of 0 was denoted as CT1 and the far side was denoted as CT2. Interaction between crack faces was assigned as "Hard" in Abaqus nomenclature for normal behavior to prevent interferences. For tangential behavior, the coefficient of friction (COF) was selected arbitrarily at 0.8 according to the friction coefficient of steel on steel for dry contact conditions (COF = 0.5-0.8). However, the heat generated due to frictional rubbing and self-weight were not

considered in this work. The shaft model was small and subjected to vibrate at high frequency thereby the self-weight was considered negligible as the previous research (55). The uncracked shaft model was globally meshed with the C3D8R elements of 0.5 mm of mesh seed for the entire model. The curvature control factor of the mesh seed was set at 0.005 to increase the mesh density of the model which directly affected the accuracy of the finite element analysis result (56). The cracked shaft was modeled with the spider-web technique being applied to the area surrounding the crack with C3D20R and C3D15, which were quadratic elements to provide a precise result. The size of the element around the crack tip was nearly 0.005 mm to acquire a converged result. However, the rest of the models were applied with C3D8R to optimize the computational time. Furthermore, both areas had a different type of element and were tied with surface-to-surface constraints. An example of model meshing on shafts is shown in Figure 5.

3. 2. Crack Characteristics and Loading Conditions

The transverse crack was one of the common cracks on a shaft that occurred frequently in a rotating shaft (57). In this study, the transverse crack was artificially created at the middle of the shaft length. The crack geometry was modeled based on a semi-elliptical crack shape with the crack length and shape factor serving as the controlled parameters. These parameters are illustrated in Figure 6.

Characteristic length of crack (α) ;

α = a/R = 0.05, 0.1, 0.25, 0.5, 0.75, 1

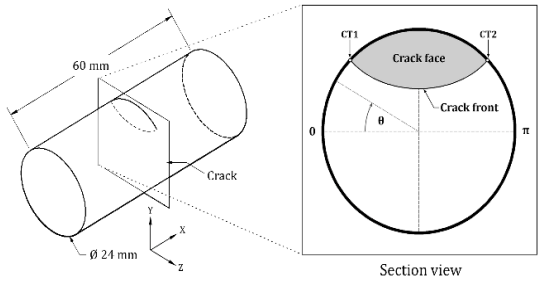

Figure 4. Isometric view of cracked shaft and cracked components

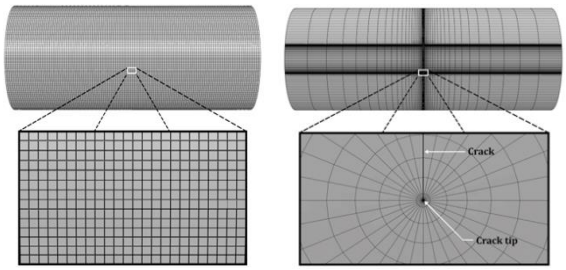

(a) Uncracked shaft (b) Cracked shaft

Figure 5. Model meshing

Shape factor of crack (β);

β = a/C = 0 (Straight crack front), 0.25, 0.5, 0.75, 1 (Circular crack front)

For the current study, the excitation directions and support conditions were varied to provide the different modes for the excited shaft. The modes of vibration depended on the direction of loading (58). The computational models consisted of two support conditions: cantilever support and fixed-end support. In the cantilever support configuration, the excitation load was applied on the free end of the shaft, referred to as axial excitation. In the fixed-end support configuration, the excitation load was applied transversely to the shaft at the middle, called transverse excitation, as shown in Figure 7. Furthermore, the diameter of the contact face for the ultrasonic transducer was measured at 45 mm.

4. TEMPERATURE-STRAIN RELATIONSHIP OF SCM440 AND TEMPERATURE PREDICTION

4. 1. Experimental Results of the Temperature-Strain Relationship

The residual stress of the

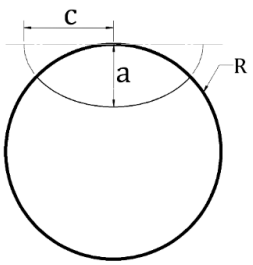

Figure 6. Controlled parameters of the semi-elliptical crack

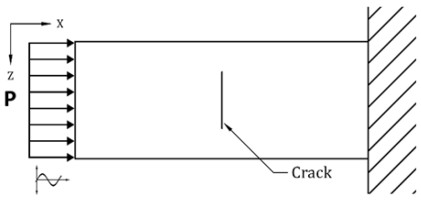

(a)

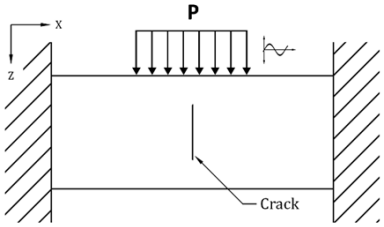

(b)

Figure 7. Excitation direction and boundary conditions on the cracked shaft; (a) Axial excitation with cantilever support, (b) Transverse excitation with fixed ends support

specimens is obtained as detailed in Table 2. The residual stress data provide a noticeable difference in the residual stress due to the different grinding directions under the surface preparation process. The larger compressive residual stress has been observed on the axis that is parallel to the direction of the grinding path. Under uniaxial tensile testing, the specimens that were ground similar to the loading direction are denoted as parallel ground and vice versa, denoted as perpendicular ground. The parallel ground specimens have slightly higher tensile stress than the perpendicular ground. The maximum difference of the ultimate tensile strength (UTS) between parallel ground and perpendicular ground specimens is approximately 40 MPa, which is less than 5%, indicating the negligible influence of the residual stress on the stress-strain curve. The average elastic modulus (E) and UTS of SCM440 steel are 201.4 GPa and 1080 MPa, respectively, as illustrated in Figure 8.

Temperatures have been observed under tensile testing, conveying the temperature increase during deformation. The temperatures increased corresponding to the strain of the tensile specimen. Considering the temperature before the necking, the temperature changes (ΔT) of the parallel ground and perpendicular ground specimens have been plotted against the true equivalent strains ($true\,\varepsilon_{eq}$) to investigate the influence of residual stress, as depicted in Figure 9. The average temperature changes were calculated individually for each case. The uncertainty of the temperature measurements on the parallel ground and perpendicular ground specimens was approximately ±0.2 °C, as shown in Figure 9a. The average temperature changes for both grinding specimens were compared to investigate the influence of residual stress, as shown in Figure 9b; the maximum difference of the temperature change between the parallel ground and perpendicular ground specimens was less than 0.07 °C. These results suggest that the residual stress had no significant influence on the temperature induced during deformation. Furthermore, the mean temperature change was calculated from the average temperature changes of both grinding conditions to describe the behavior of temperature during deformation.

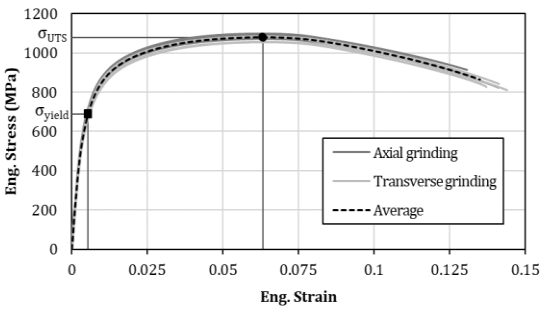

Figure 8. Engineering stress-strain curve of SCM440 specimens

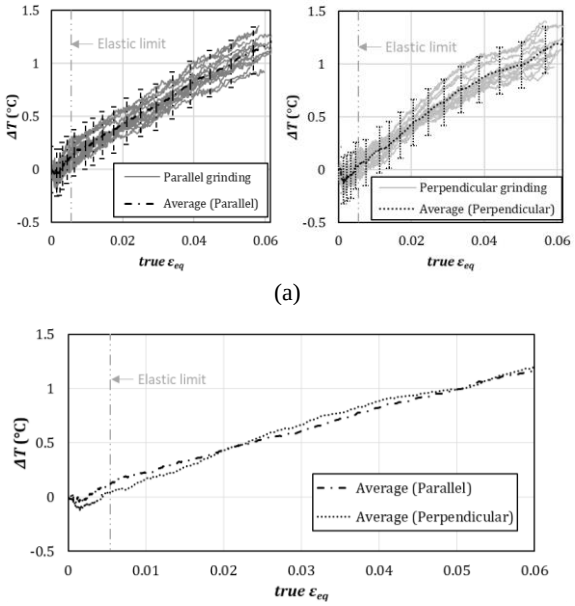

(a)

(b)

Figure 9. Temperature during deformation prior to necking, (a) Uncertainty of the temperature measurement, (b) Temperature variations under different grinding directions

TABLE 2. Residual stress at P1, P2, and P3

Grinding direction	No.	Y-axis P1	Y-axis P2	Y-axis P3	X-axis P1	X-axis P2	X-axis P3
Y-axis (Parallel)	1	-366.5	-364.5	-371	-134.5	-137.5	-132.5
	2	-362	-358	-364	-79	-88.5	-102.5
	3	-365	-356.5	-379.5	-134	-103.5	-116.5
	4	-384	-373.5	-357.5	-102.5	-103.5	-91
	5	-376	-370	-356.5	-126.5	-139.5	-139
X-axis (Perpendicular)	6	-58.5	-60	-44.5	-361	-372	-364
	7	-122	-112	-124.5	-352	-338	-347
	8	-56	-55	-44	-348	-383	-375
	9	-133	-106	-102	-349.5	-351	-351.5
	10	-49.5	-42.5	-59	-372.5	-365	-359

From the observation, the behavior of the mean temperature change exhibits a relatively low-temperature change with a fluctuation in the beginning of elastic region and the temperature increases noticeably along the strain-hardening region, indicating the temperature changes substantially during plastic deformation.

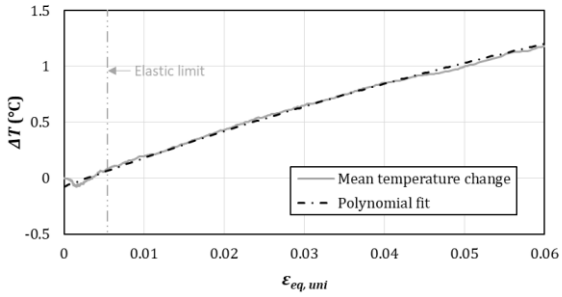

Figure 10. Temperature-strain relationship

Furthermore, the mean temperature change is plotted against true equivalent strain prior to the necking, denoted as uniform equivalent strain ($\varepsilon_{eq,uni}$), to construct the temperature-strain relationship, as demonstrated in Figure 10. The second degree of the polynomial curve fitting has good fit with the relationship curve, which has a confidence of R^2 = 0.9985. From curve fitting, the polynomial regression can be expressed as Equation 4:

$$\Delta T = -86.515\varepsilon_{eq,uni}^2 + 26.437\varepsilon_{eq,uni} - 0.0758 \quad (4)$$

4. 2. Prediction of Temperature Based on the Temperature-Strain Relationship The developed relationship was applied for the temperature prediction of the specimen under tensile testing. Similar material was machined into a standard tensile specimen with a circular cross-section of gauge diameter 6 mm and 25 mm long of gauge length, as shown in Figure 11a. These dog-bone specimens were painted in black to prevent reflection from ambient light. Moreover, an extensometer and FLIR A655sc infrared (IR) camera were also equipped in the test, as shown in Figure 11b. Non-Uniformity Correction (NUC) was set for the IR camera to automatically improve the temperature reading, which provided more accuracy during the record. The cross-head of the testing machine was set to 0.5 mm/min. The records were stopped after the specimen reached the necking stage to prevent accidental damage to the IR camera lens. Meanwhile, the computational model was additionally created to investigate the strain behavior during the test. The configurations were set accordingly to the constraints and boundary conditions of the experiment. As a result, the strain alteration of the tensile specimens obtained from the experiment and simulation are plotted to unveil the strain behavior during deformation, as observed in Figure 12. Under fixed-speed controlled deformation, the true strains of the tensile specimens have corresponding behavior, which barely changed under the elastic deformation and increased exponentially in the plastic deformation.

Regarding the temperature, the initial temperatures were measured prior to the test using an IR camera. The temperature behavior from the IR camera was investigated using ResearchIR software. The side-by-side view between the temperature gradient and the computational strain distribution is displayed simultaneously in Figure 13a, which reveals a comparable color contour. Hence, the strains were sequentially substituted into Equation 4 and Equation 1 for determining the predicted temperatures. The predicted temperatures were plotted to compare with Figure 13b demonstrates a significant correlation between the temperature predictions and the actual temperature during deformation. The accuracy of these predictions is detailed in Table 3. The maximum absolute error observed among the multiple tests was approximately 0.4 °C, which suggests a close agreement. These findings suggest the potential usability of the developed temperature-strain relationship for temperature prediction based on strain alteration with a disagreement of less than 1.5%. The results provide compelling evidence that the deformation temperature can be estimated effectively when the corresponding strain alteration is known. It is important to note that the developed relationship is specifically applicable to SCM440 material with a constant deformation speed of 0.5 mm/min.

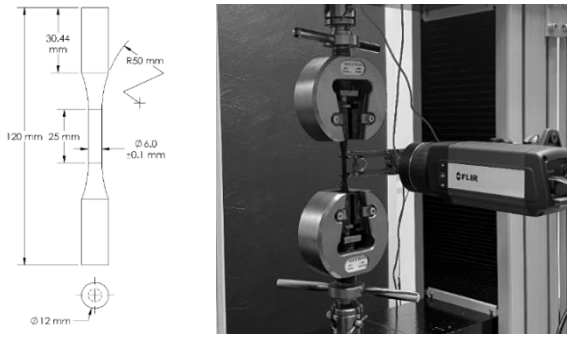

(a) (b)

Figure 11. Experimental temperature prediction setup

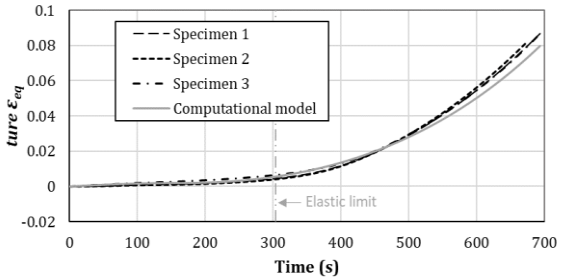

Figure 12. Strain alteration prior to necking the actual temperature within the gauge section, as presented in Figure 13b

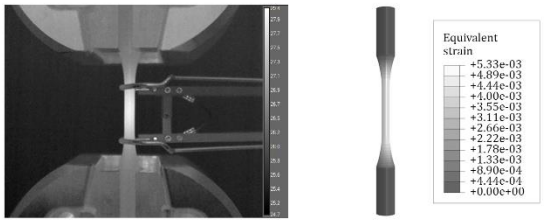

(a)

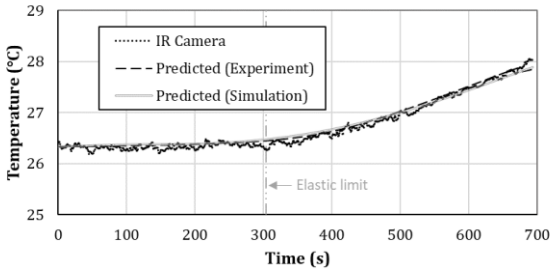

(b)

Figure 13. Temperature prediction, (a) Temperature and strain distribution at t= 630 s, (b) Comparison of temperature predictions

TABLE 3. Accuracy of temperature prediction under uniaxial tensile testing

No.	Initial temperature (°C)	Maximum error			
		Absolute (°C)		Percentage (%)	
		EXP.	FEM.	EXP.	FEM.
1	26.405	0.220	0.218	0.785	0.829
2	26.533	0.409	0.384	1.489	1.436
3	26.442	0.311	0.370	1.132	1.382

5. STRAIN RESPONSE OF THE CRACKED AND UNCRACKED SHAFT UNDER EXCITATION

5. 1. Computational Investigation of Uncracked Shaft The computational results show the response of the stress field generated under excitation. Stress is generated following the deformation of the vibrated shaft. The shafts vibrate back and forth in different directions depending on the excitation direction. For example, axial vibration occurs under the axial excitation condition and transverse vibration occurs under the transverse excitation condition. Under the investigations, stresses were found within the yield limit, which could be directly converted into the corresponding strains using Hook's law (Equation 3). The behavior of stress distributions varies between the two excitation conditions due to the dissimilarity of the stress propagation. Under axial excitation, stress propagates along the length of the shaft, creating a longitudinal stress distribution. In contrast, stress is distributed from the top to the bottom of the shaft under transverse excitation, resulting in lateral stress distribution. These observations are displayed in Figure 14, which shows the distinct patterns of strain contour under each excitation condition. At the middle of the shaft where the stress is fluently distributed under both excitations, strain responses are observed, as shown in Figure 15a, which reveals the dynamic behavior of strain. The response between both excitations shows slight phase shifting and varying amplitudes. Examining the first peak of the responses that display close characteristics, the circumferential surface strains under both excitations are plotted to display the strain distribution, as depicted in Figure 15b. Under axial excitation, the strain distribution is uniform along the shaft circumference. On the contrary, the strain under transverse excitation exhibits a distinct pattern.

It is the highest at an angular displacement (θ) of 0, where excitation takes place and reaches its lowest at $\theta = \pi/2$. Then, the strain increases gradually as the angular displacement progresses towards $\theta = \pi$. This finding highlights the significant influence of the excitation source on strain generation in the excited shaft under transverse excitation, particularly in the vicinity of the excitation location. The excitation source plays a notable role in elevating strain levels, and it is crucial to recognize the influence of the excitation source on strain generation during analytic consideration. In this study, the strains at the opposite side of the excitation ($\theta = \pi$) for transverse excitation are considered to minimize the direct influence of the excitation source on the strain measurement. From the observation, the maximum strain generations due to the deformation under the excitations of uncracked shafts were found to be 3.89×10^{-9} and 4.72×10^{-9} for the axial and transverse excitation, respectively.

5. 2. Experimental Investigation of Uncracked Shaft This section explains the experiments conducted to observe the deformation of the uncracked shaft under

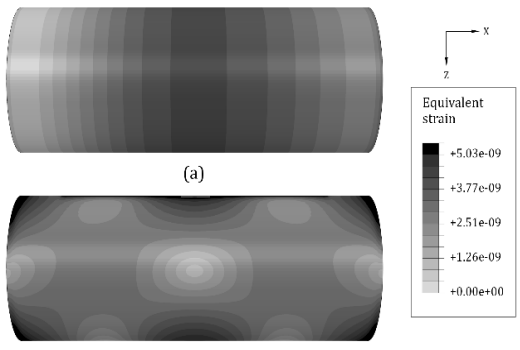

(a)

(b)

Figure 14. Top view of the strain distribution on the uncracked shaft under excitation, (a) Axial excitation, (b) Transverse excitation

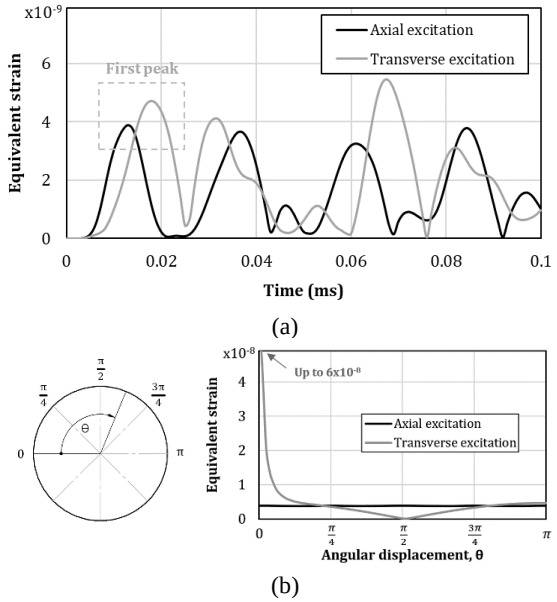

Figure 15. Strain responses of the uncracked shaft at the middle, (a) Example of the strain response at $\theta = \pi$ (b) Circumferential strain under excitations

excitation. For instance, in the case of the transverse excitation, the jig and fixture were designed to securely hold the uncracked shaft in fixed-ends support condition, as shown in Figure 16. An ultrasonic transducer was positioned on the slider body of the linear guide rail, which was utilized to minimize the influence of gravitational force and apply excitation to the side of the shaft. The slider body was connected to an adjustable pin, and a helical spring was incorporated to allow for the adjustment of contact pressure between the transducer and the shaft. The contact pressure can be calculated based on the compressive length and stiffness of the spring, which was determined to be 2.8 N/mm under the compression test. The designed jig and fixture were clamped securely onto a rigid table, with a rubber plate placed in between to isolate the system from the surrounding environment. To measure the deformation on the surface of the shaft during excitation, a 3D digital image correlation (DIC) system was utilized. The system was set to record real-time data at a maximum resolution of 40 frames per second. Before conducting the test, an SCM440 shaft with a diameter similar to the one used in the computational study was prepared by spraying a pattern for surface mapping and marking a reference point for precise analysis. Meanwhile, the computational model used in this section was modified to match the experimental setup. An initial load was applied to simulate the preloading caused by the contact pressure of the ultrasonic transducer. The load was offset by 19.7 N, corresponding to a 7 mm compression of the spring in the experimental setup. However, the other configurations remained the same as in the previous setups.

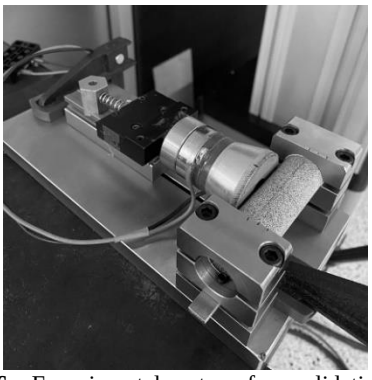

Figure 16. Experimental setup for validation of the computational results

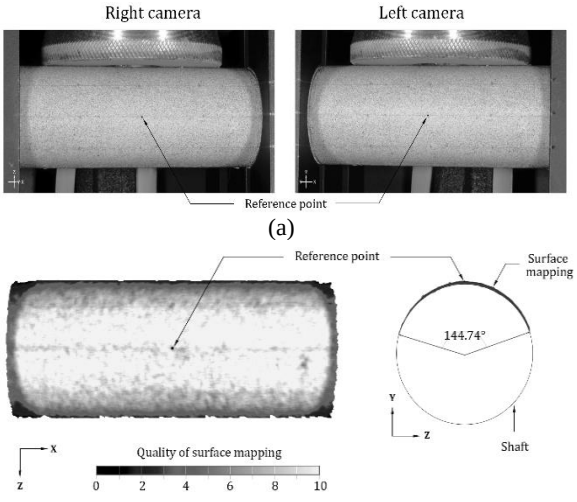

Figure 17. Digital image-processing using GOM correlation software, (a) Images captured by the GOM DIC system (b) Quality and angular displacement of the surface mapping

Under the investigation, the magnitudes of deformation on the shaft surface were observed in the response during excitation. For the experimental data, the different angles of the excited shaft were captured using the dual camera setup on the DIC system, as displayed in Figure 17a. Both images were used to construct a 3D surface model based on the prepared surface pattern, thus facilitating the measurement of surface changes. The shaft surface pattern was mapped using the GOM correction software for digital image processing. The surface mapping captured approximately 144° of angular displacement. The quality of the mapping was examined and rated on a scale from 0 to 10, with 10 indicating high quality and 0 indicating poor quality. The results indicated that the mapping exhibited high quality around the front part of the shaft, as illustrated in Figure 17(b). Furthermore, the magnitude of deformation was normalized with respect to the reference point located in the middle of the shaft.

When comparing the results, the steady state was considered where the response exhibited a consistent behavior. Figure 18 displays the contour of the magnitude of deformation from both experimental and computational investigations, revealing the similar behavior of the shaft. A significant deformation was observed in the middle region, which gradually decreased toward the fixed ends. The experimental investigation showed slightly higher deformation around the fixed-end supports compared to the computation, indicating a small translation motion of the designed fixture during excitation. Additionally, the magnitude of deformation along the circumference at the middle of the shaft was also investigated, as depicted in Figure 19. The experimental results showed a slight difference compared to the computational results, particularly in the vicinity of the excitation source. The magnitude of deformation observed in the experiment was higher than what was predicted by computation. The difference could be attributed to several factors, including potential issues with surface mapping quality at the edge of the shaft or the presence of a non-rigid fixture at the fixed ends. The percentage error prior to the angular displacement of $\pi/4$ was up to 10%. Nevertheless, the percentage error beyond the angular displacement of $\pi/4$ was less than 5%, indicating good agreement with the computational results beyond the angular displacement of $\pi/4$. Besides, both responses demonstrated similar behavior, exhibiting consistent patterns of deformation with high magnitudes of deformation near the excitation source and lower magnitudes on the opposite side. Based on the comparison of the shaft response in both investigations, the behaviors exhibited by the shaft under excitations are well-correlated, particularly in the middle region and the farther region of excitation. These findings strongly support the effectiveness of the current configurations of

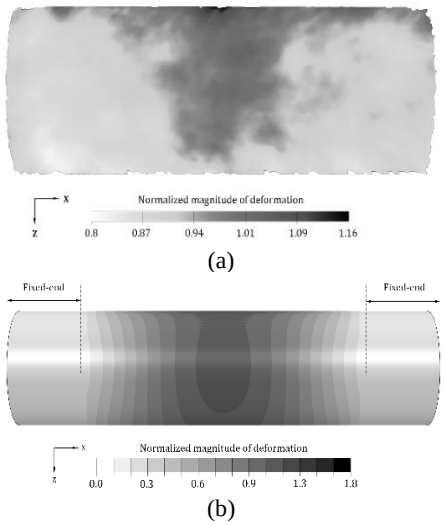

Figure 18. Deformation magnitude of the uncracked shaft under transverse excitation, (a) Experiment, (b) FEM

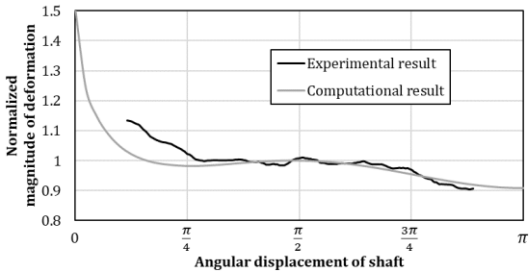

Figure 19. Comparison of deformation magnitude along the shaft circumference

the computational model for studying the shaft response under excitation.

Working under low-power excitation, especially for ultrasonic applications, is challenging because of the sensitivity and rapidity. Accurate measurement of alterations requires the use of highly responsive equipment with high sensitivity. In this experiment, the intention was to employ an infrared (IR) camera with a developed temperature prediction technique for temperature measurement.

However, the strain responses of the uncracked shaft under the excitations studied indicated that the technique was not yet fully applicable. The computational investigation revealed extremely low strain responses under excitations significantly below the yield point. Additionally, the DIC system could not accurately capture these low-strain alterations due to its limitations. The strain contour of the excited shaft under the computational investigation is displayed in Figure 20, including temperature prediction using the temperature-strain relationship, assuming a constant initial temperature of 25 °C. The predicted temperature was observed to be approximately 24.92°C ± 0.0001%. The maximum temperature difference was much less than the thermal sensitivity of the currently used IR camera (0.03 °C). Temperature changes were unnoticeable on the IR camera, as expected. The results indicated that the excitation power applied by the low-power ultrasonic cleaning transducer was insufficient, implying the need for the enhancement of excitation power to summarize the changes in practical measurement.

The temperature prediction technique based on strain alteration is likely to be applicable for deformation detection. However, the temperature of the uncracked shaft under excitation was well below the sensitivity threshold of the IR camera, resulting in undetectable changes. Nevertheless, the developed temperature prediction technique has the potential to be effective in estimating the temperature changes when utilized with a high-sensitivity IR camera and accurate predictions of the deformation are available. Hence, the study aims to investigate the strain response on the cracked shaft. The computational model of the uncracked shaft is extended, including a surface crack at the middle of the shaft.

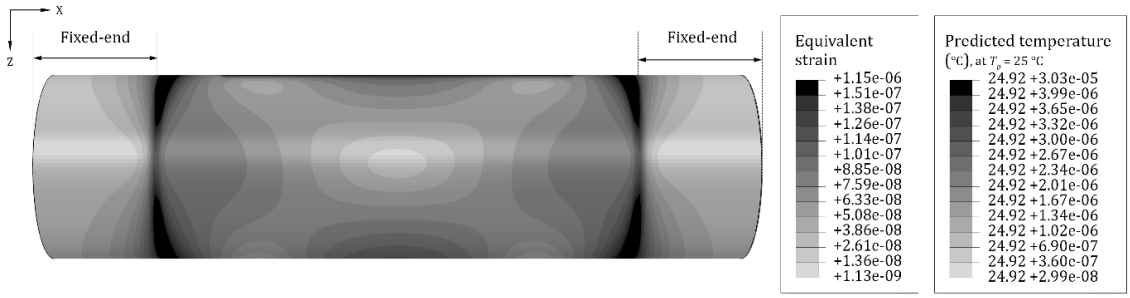

Figure 20. Temperature prediction of the uncracked shaft under the transverse excitation

5. 3. Extended Model for Investigation of Cracked Shaft During the investigation of the extended model for the cracked shaft, plasticity was not observed. The stresses under excitation remain within the yield limit of the material. Figure 21 displays the strain distribution under axial and transverse excitations, revealing a slightly different contour from the previous investigation of the uncracked shaft due to the meshing adjustment in the outside crack area to optimize computational time. For the vicinity of the middle region where the crack is located, the strain is mainly concentrated around the crack tips, where it is noticeably higher compared to the uncracked shaft. However, no crack propagation was observed. Considering the behavior of the strain around the crack tips under the stress flow due to excitation, the localized strains at both tips of the crack are simultaneously equivalent under the axial excitation. In contrast, strains under the transverse excitation exhibit time-dependent variations in strain generation at the crack tips. The strain generation at the crack tip oscillates over time showing periodic pattern, with higher strain observed initially at the tip closer to the excitation and then gradually reduced with higher strain being observed at the tip located farther away from the excitation. The crack tip at the far side of the excitation (CT2) is selected for the investigation of strain generation to minimize the influence of the excitation source, which was previously found in the investigation of the uncracked shaft under the excitation. The strain generation at the tip of the cracked shaft is significantly higher than the maximum strain generation of the uncracked shaft. The strains are normalized with the maximum strain observed in the uncracked shaft. Sequentially, the normalized strains are plotted against the characteristic parameters of the crack under various excitation conditions aiming to investigate the influence of the crack geometry on strain alteration at the crack tips. The results of the analysis are presented in Figure 22.

Figure 22 illustrates the influence of crack geometry on the strain alteration surrounding the crack tip. Larger cracks result in a higher strain, as demonstrated by a circular crack with a characteristic length of 0.75 (β = 1,

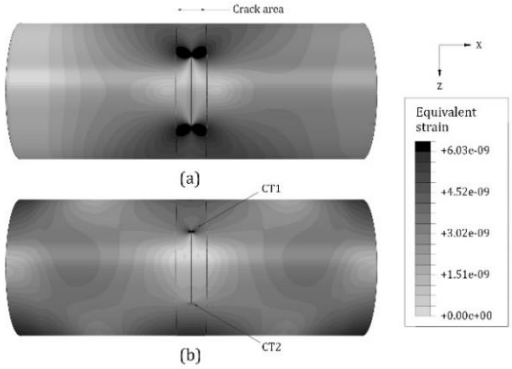

Figure 21. Example of the strain distribution on the cracked shaft under excitation, (a) Axial excitation on the circular cracked shaft (β = 1) with α = 0.5 (b) Transverse excitation on the circular cracked shaft (β = 1) with α = 0.5

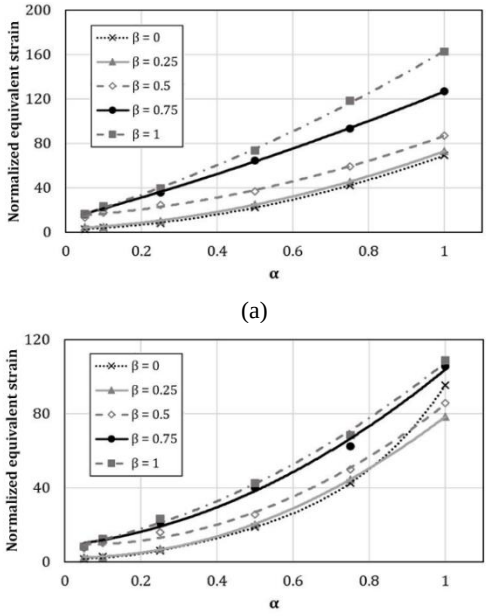

Figure 22. Influence of the crack geometry on strain alteration beyond the crack tip, (a) Axial excitation, (b) Transverse excitation

α = 0.75) exhibiting greater strain alteration compared to a circular crack with a characteristic length of 0.5 (β = 1, α = 0.5) under excitation. Besides, the circular crack front (β = 1) demonstrates the highest strain during excitation, while the straight front (β = 0) exhibits the lowest strain under observation. This behavior consistently shows a similar pattern, except for the straight front crack with α = 1 under transverse excitation. The strain of the straight front crack is noticeably higher than the crack with β = 0.5 at a similar characteristic length of α = 1. To understand the disparity, a comprehensive analysis was carried out by plotting the strain alteration over time for all examined crack geometries with α = 1 under the transverse excitation. Figure 23a reveals the extreme shift of phases on the straight front crack (β = 0), while the other crack fronts (β = 0.25 to 1) exhibit a slight shift of phases in the response. The reason for the massive phase shifting of the straight front crack (β = 0) shaft under the transverse excitation may arise from the alignment of the crack with the excitation direction. One of the tips of this crack configuration (β = 0, α = 1) locates directly under the excitation source, causing the load to transfer through the crack front to the other tip where the measurements are taken. Figure 23b illustrates the layout of the crack shaft, which contains a straight front with α = 1 under transverse excitation. The crack is aligned in line with the excitation direction, which could be the major cause of the phase shifting that leads to the difference in the strain behavior of the straight front crack (β = 0) with α = 1 under transverse excitation, highlighting the alignment of the excitation source must be considered in the analysis for estimation purpose. Overall, the crack geometry of the circular cracked shaft influenced the alteration in strain surrounding the crack tip, which increased with the shape factor (β) and the characteristic length (α). These findings align with prior research involving surface semi-elliptical cracked shafts. For instance, Carpinteri, A. unveiled the relationship between the geometry correction factor (FI) and the characteristic length of the stress intensity factor in the circular cracked shaft under cyclic axial loading (59). The geometry factor of the opening mode stress intensity factor for a surface crack in the solid cylinder can be expressed as Equation 5 (60):

$$F_I = \frac{K_I}{\sigma\sqrt{\pi a}}; F_I \propto \frac{1}{\sigma} \quad (5)$$

where the coefficient 'a' represented the crack depth. The relationship between the geometry factor and the characteristic length revealed a lower geometry factor with an increasing shape factor as depicted in Figure 24. Comparing this relationship with the strain alteration and characteristic length relationship found in the current study, it shows that the behavior of strain corresponds with Carpinteri's work. Since the lower geometry factor indicated the higher stress as it was inversely proportional according to Equation 5 and stress was directly proportional to strain within the elastic which was also found in the cracked shaft responses of this analysis. These findings indicate that strain alteration was higher with the increasing shape factor, similar to the findings of the current study as discussed. Other studies have shown similar results of the geometry factor and the characteristic length relationship as following literature (60-63).

In addition, the temperature prediction technique is applied to estimate the temperature from the strain of the excited cracked shaft to illustrate the surface temperature prediction. The technique is performed on the cracked shaft with a circular front and a characteristic length of 1 (β = 1, α = 1), which has been observed as the crack geometry generating the highest strain under both excitation conditions. Figure 25 displays the strain contour with the predicted corresponding temperature.

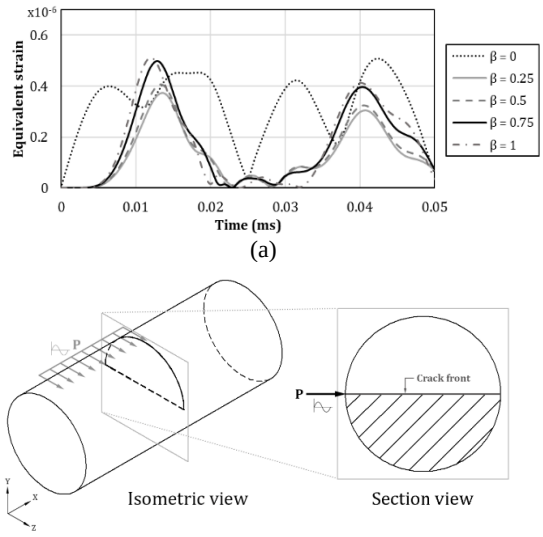

Figure 23. Responses of the cracks with α = 1 under transverse excitation, (a) Strain responses of the different crack front (b) Section view of the straight front crack under excitation

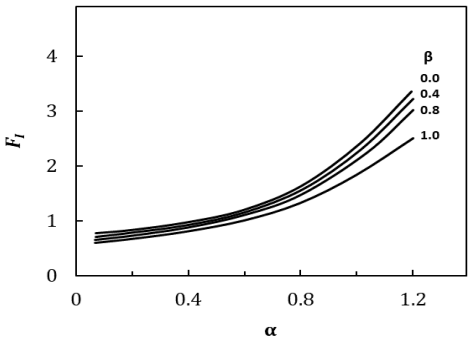

Figure 24. Geometry correction factor variation near crack tips along the crack characteristic

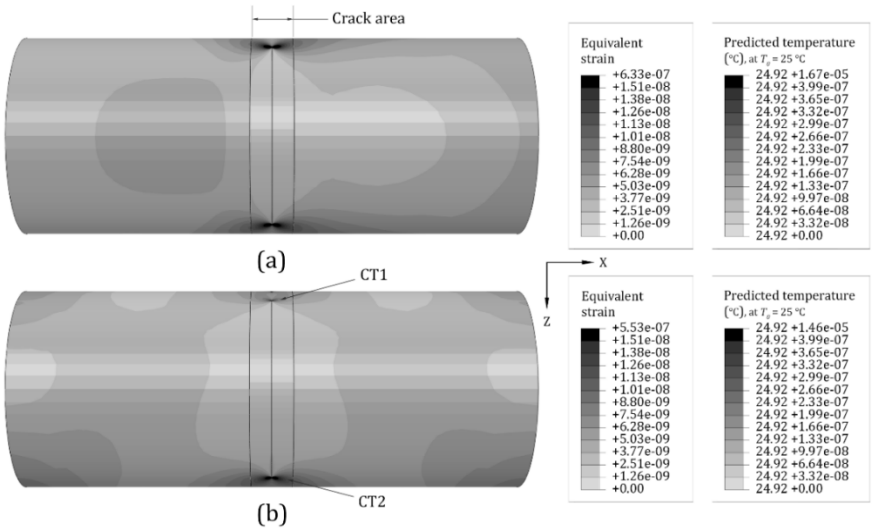

Figure 25. Strain contour and predicted corresponding temperature, (a) Axial excitation of the circular cracked shaft (β = 1) with α = 1, (b) Transverse excitation of the circular cracked shaft (β = 1) with α = 1

The maximum temperature differences are $1.67x10^{-5}$ °C and $1.46x10^{-5}$ °C for axial and transverse excitation, respectively. The temperature differences show a significant increase compared to the predicted temperatures of the maximum strain on the uncracked shaft ($1.03x10^{-7}$ °C for axial excitation and $1.25x10^{-7}$ °C for transverse excitation), with percentage increments of $1.63x10^{4}$ % and $1.17x10^{4}$ %, respectively.

Despite the increment, the temperature changes in the cracked shaft are still hardly measurable in practice, emphasizing the insufficient excitation power from the currently used ultrasonic transducer.

The improvement of excitation power and the use of a high-sensitivity IR camera are strongly recommended to enhance the effectiveness of the temperature prediction technique in practical applications. Estimating the defective area is achievable by leveraging the strain distribution around the crack through the utilization of an IR camera to capture the corresponding temperature .

It's crucial to emphasize that the temperature prediction technique was developed within a controlled environment in a research laboratory. Temperature variations can potentially influence material stiffness and heat transfer (64). While conducting, the impact of the ambient conditions, especially the surrounding temperature, should be taken into account. Consequently, the technique may not be well-suited for use in hot-working conditions, where significant changes in material properties occur and are affected by thermal radiation from surrounding components. In such conditions, both of the temperature detectability and the prediction accuracy may be compromised.

In contrast, the technique appears more suitable for natural ambient conditions, where temperature fluctuations are relatively modest compared to the extreme conditions of the hot-working conditions. Nevertheless, it's essential to acknowledge that even in natural ambient conditions, the external variables like sunlight and wind can influence temperature-induced changes, affecting the accuracy of temperature predictions.

For a comprehensive understanding, further studies should be undertaken to improve this technique and observe its limitations in real-world inspection scenarios.

6. CONCLUSION

This study carried out observations on the deformation-induced heating mechanism of SCM440 material. The observations revealed a correlation between temperature and deformation strain, where the temperature increases along the strain alteration. The results of the study suggest that the temperature can be predicted from the strain using the temperature-strain relationship. The developed temperature prediction technique can be applied to estimate the temperature of tensile specimens, demonstrating good predictability with a maximum absolute error of approximately 0.4 °C among multiple tests. Moreover, computational-based studies were involved in this work. Both cracked and uncracked SCM440 shafts were investigated for strain responses under ultrasonic excitation. The computational model was tested under different control variables, including

crack shapes, sizes, supports, and excitation conditions to investigate their influence on the strain responses. The experimental validation exhibited good agreement for the computational model with the shaft response under excitation. The results for the cracked shaft revealed significantly higher strain responses compared to the uncracked shaft, with the circular front crack exhibiting the greatest strain generation under any excitation conditions. The temperature prediction technique was also applied to estimate the temperature gradient from the strain distribution of shaft responses. However, the strain responses under the studies were very small with an excitation force of 0.35 N generated by the low-power ultrasonic cleaning transducer employed in this work, resulting in undetectable temperature changes in practice. To effectively utilize this prediction technique, improvements in the excitation power and the use of a high-sensitivity IR camera are required. Based on both investigations, the results strongly suggest that the temperature prediction technique can effectively estimate defective areas due to the strain distribution around a crack. Further studies should be conducted to optimize the temperature prediction based on the strain alteration technique for practical applications.

7. ACKNOWLEDGMENT

The research on Development of Temperature-Strain Prediction Based on Deformation-Induced Heating Mechanism in SCM440 Surface Cracked Shaft under Ultrasonic Excitation by King Mongkut's University of Technology North Bangkok (KMUTNB) received funding support from the National Science, Research and Innovation Fund (NSRF) (KMUTNB-FF-65-65).

8. REFERENCES

1. Morbidini M, Cawley P, Barden T, Almond D, Duffour P. Prediction of the thermosonic signal from fatigue cracks in metals using vibration damping measurements. Journal of Applied Physics. 2006;100(10). 10.1063/1.2361091
2. Mendioroz A, Martínez K, Celorrio R, Salazar A. Characterizing the shape and heat production of open vertical cracks in burst vibrothermography experiments. NDT & E International. 2019;102:234-43. 10.1016/j.ndteint.2018.12.006
3. Reifsnider K, Henneke EG, Stinchcomb W. The mechanics of vibrothermography. Mechanics of nondestructive testing. 1980:249-76. 10.1007/978-1-4684-3857-4_12
4. Favro L, Han X, Ouyang Z, Sun G, Sui H, Thomas R. Infrared imaging of defects heated by a sonic pulse. Review of scientific instruments. 2000;71(6):2418-21. 10.1063/1.1150630
5. Shih Y-S, Chen J-J. Analysis of fatigue crack growth on a cracked shaft. International Journal of Fatigue. 1997;6(19):477-85. https://api.semanticscholar.org/CorpusID:136058376
6. Chowdhury P, Sehitoglu H. Mechanisms of fatigue crack growth–a critical digest of theoretical developments. Fatigue & Fracture of Engineering Materials & Structures. 2016;39(6):652-74. 10.1111/ffe.12392
7. Stephens RI, Fatemi A, Stephens RR, Fuchs HO. Metal fatigue in engineering: John Wiley & Sons; 2000.
8. Zangeneh S, Ketabchi M, Kalaki A. Fracture failure analysis of AISI 304L stainless steel shaft. Engineering Failure Analysis. 2014;36:155-65. 10.1016/j.engfailanal.2013.09.013
9. Zhao L-H, Xing Q-K, Wang J-Y, Li S-L, Zheng S-L. Failure and root cause analysis of vehicle drive shaft. Engineering Failure Analysis. 2019;99:225-34. 10.1016/j.engfailanal.2019.02.025
10. Chatterton S, Pennacchi P, Vania A, Rubio P. Analysis of the periodic breathing of a transverse annular crack propagated in a real rotating machine. Engineering Failure Analysis. 2019;99:126-40. 10.1016/j.engfailanal.2019.02.029
11. Mayton D, Spencer F, Alvarez C, editors. Characterizing the effects of sonic IR variables on turbine disk inspection using a design of experiments approach. AIP Conference Proceedings; 2005: American Institute of Physics. 10.1063/1.1916736
12. Holland SD. Thermographic signal reconstruction for vibrothermography. Infrared Physics & Technology. 2011;54(6):503-11. 10.1016/j.infrared.2011.07.004
13. Gao C, Meeker WQ, Mayton D. Detecting cracks in aircraft engine fan blades using vibrothermography nondestructive evaluation. Reliability Engineering & System Safety. 2014;131:229-35. 10.1016/j.ress.2014.05.009
14. Szwedo M, Pieczonka L, Uhl T, editors. Application of vibrothermography in nondestructive testing of structures. 6th European Workshop on Structural Health Monitoring; 2012.
15. DiMambro J, Ashbaugh D, Nelson CL, Spencer FW, editors. Sonic infrared (IR) imaging and fluorescent penetrant inspection probability of detection (POD) comparison. AIP Conference Proceedings; 2007: American Institute of Physics. 10.1063/1.2718008
16. Jia Y, Tang L, Xu B, Zhang S. Crack detection in concrete parts using vibrothermography. Journal of Nondestructive Evaluation. 2019;38:1-11. 10.1007/s10921-019-0562-0
17. Luong MP. Infrared thermovision of damage processes in concrete and rock. Engineering Fracture Mechanics. 1990;35(1-3):291-301. 10.1016/0013-7944(90)90207-W
18. Tian G, Zhang W, Jin GF, Zhu L, Yang ZW. Detection of Ceramic Material Crack Defect Based on the Ultrasonic Infrared Thermal Wave Technique. Advanced Materials Research. 2013;791:949-53. 10.4028/www.scientific.net/AMR.791-793.949
19. Vaddi JS, Holland SD, Kessler MR. Loss modulus measurement of a viscoelastic polymer at acoustic and ultrasonic frequencies using vibrothermography. Measurement. 2021;168:108311. 10.1016/j.measurement.2020.108311
20. Katunin A, Wronkowicz-Katunin A, Wachla D. Impact damage assessment in polymer matrix composites using self-heating based vibrothermography. Composite Structures. 2019;214:214-26. 10.1016/j.compstruct.2019.02.003
21. Bolu G, Gachagan A, Pierce G, Harvey G. Reliable thermosonic inspection of aero engine turbine blades. Insight-Non-Destructive Testing and Condition Monitoring. 2010;52(9):488-93. 10.1784/insi.2010.52.9.488
22. Morbidini M, Cawley P. The detectability of cracks using sonic IR. Journal of Applied Physics. 2009;105(9). 10.1063/1.3125444
23. Ibarra-Castanedo C, Genest M, Guibert S, Piau J-M, Maldague XP, Bendada A, editors. Inspection of aerospace materials by pulsed thermography, lock-in thermography, and vibrothermography: a comparative study. Thermosense XXIX; 2007: SPIE. 10.1117/12.720097
24. Glass III SW. Guide to Nondestructive Evaluation Techniques. Nondestructive Evaluation of Materials: ASM International; 2018. p. 3-7.

25. Renshaw J, Chen JC, Holland SD, Thompson RB. The sources of heat generation in vibrothermography. Ndt & E International. 2011;44(8):736-9. 10.1016/j.ndteint.2011.07.012
26. Holland SD, Uhl C, Ouyang Z, Bantel T, Li M, Meeker WQ, et al. Quantifying the vibrothermographic effect. NDT & E International. 2011;44(8):775-82. 10.1016/j.ndteint.2011.07.006
27. Mabrouki F, Thomas M, Genest M, Fahr A. Frictional heating model for efficient use of vibrothermography. NDT & E International. 2009;42(5):345-52. 10.1016/j.ndteint.2009.01.012
28. Renshaw J, Holland SD, Thompson RB. Measurement of crack opening stresses and crack closure stress profiles from heat generation in vibrating cracks. Applied Physics Letters. 2008;93(8). 10.1063/1.2976310
29. Rizi AS, Hedayatrasa S, Maldague X, Vukhanh T. FEM modeling of ultrasonic vibrothermography of a damaged plate and qualitative study of heating mechanisms. Infrared Physics & Technology. 2013;61:101-10. 10.1016/j.infrared.2013.07.011
30. De Cazenove J, Rade D, De Lima A, Araújo C. A numerical and experimental investigation on self-heating effects in viscoelastic dampers. Mechanical Systems and Signal Processing. 2012;27:433-45. 10.1016/j.ymssp.2011.05.004
31. Singh V, Sangle K. Analysis of vertically oriented coupled shear wall interconnected with coupling beams. HighTech and Innovation Journal. 2022;3(2):230-42. 10.28991/HIJ-2022-03-02-010
32. El Yassari S, El Ghoulbzouri A. Numerical simulation of fiber-reinforced concrete under cyclic loading using extended finite element method and concrete damaged plasticity. International Journal of Engineering, Transactions A: Basics. 2023;36(10):1815-26. 10.5829/IJE.2023.36.10A.08
33. Talouti S, Benzerga D, Abdelkader H. Numerical Investigations of Damage Behaviour at the Weld/Base Metal Interface. International Journal of Engineering, Transactions C: Aspects. 2022;35(12):2337-43. 10.5829/IJE.2022.35.12C.09
34. Gholami P, Kouchakzadeh MA, Farsi M. A continuum damage mechanics-based piecewise fatigue damage model for fatigue life prediction of fiber-reinforced laminated composites. International Journal of Engineering, Transactions AC: Aspects. 2021;34(6):1512-22. 10.5829/IJE.2021.34.06C.15
35. Salarvand A, Poursaiedi E, Azizpour A. Probability Approach for Prediction of Pitting Corrosion Fatigue Life of Custom 450 Steel. International Journal of Engineering, Transactions A: Basics. 2018;31(10):1773-81. 10.5829/IJE.2018.31.10A.21
36. Boussalih F, Fedaoui K, Zarza T. Chaboche Model for Fatigue by Ratcheting Phenomena of Austenitic Stainless Steel under Biaxial Sinusoidal Loading. Civil Engineering Journal. 2022;8(3):505-18. 10.28991/CEJ-2022-08-03-07
37. Cuong DQ, Chinh VD. Estimation of Overall Fatigue Life of Jack-up Leg Structure. Civil Engineering Journal. 2022;8(03). 10.28991/CEJ-2022-08-03-06
38. Jeong J-I, Kim J-H, Choi S-G, Cho YT, Kim C-K, Lee H. Mechanical properties of white metal on scm440 alloy steel by laser cladding treatment. Applied Sciences. 2021;11(6):2836. 10.3390/app11062836
39. Kapoor R, Nemat-Nasser S. Determination of temperature rise during high strain rate deformation. Mechanics of materials. 1998;27(1):1-12. 10.1016/S0167-6636(97)00036-7
40. Lamboul B, Passilly F, Roche J-M, Balageas D, editors. Ultrasonic vibrothermography using low-power actuators: An impact damage detection case study. AIP Conference Proceedings; 2015: American Institute of Physics. 10.1063/1.4914626
41. Xu C, Xie J, Zhang W, Kong Q, Chen G, Song G. Experimental investigation on the detection of multiple surface cracks using vibrothermography with a low-power piezoceramic actuator. Sensors. 2017;17(12):2705. 10.3390/s17122705
42. Liu P, Xu C, Zhang Y, Qin Y, Xu Y, Xie J, et al. Low-power vibrothermography detection technique for surface cracks on composite sucker rod. Smart Materials and Structures. 2023;32(3):035034. 10.1088/1361-665X/acb979
43. Anderson TL. Fracture mechanics: fundamentals and applications: CRC press; 2017.
44. Tada H, Paris P, Irwin G. The stress analysis of cracks handbook, Del Research Corporation, St. Louis, Missouri. 1973.
45. Abbasnejad A, Moradi G. Frictional Strain Hardening-softening in Experimental and Numerical Investigation of Arching Effect. International Journal of Engineering, Transactions B: Applications. 2015;28(2):180-9. 10.5829/idosi.ije.2015.28.02b.03
46. Shahraini SI, Kadkhodayan M. Ratcheting Analysis of Steel Plate under Cycling Loading using Dynamic Relaxation Method Experimentally Validated. International Journal of Engineering, Transactions C: Aspects. 2021;34(6):1530-6. 10.5829/ije.2021.34.06c.17
47. McClung R, Sehitoglu H. On the finite element analysis of fatigue crack closure—1. Basic modeling issues. Engineering fracture mechanics. 1989;33(2):237-52. 10.1016/0013-7944(89)90027-1
48. De-Andrés A, Pérez J, Ortiz M. Elastoplastic finite element analysis of three-dimensional fatigue crack growth in aluminum shafts subjected to axial loading. International Journal of Solids and Structures. 1999;36(15):2231-58. 10.1016/S0020-7683(98)00059-6
49. Rigby S, Tyas A, Bennett T. Elastic–plastic response of plates subjected to cleared blast loads. International Journal of Impact Engineering. 2014;66:37-47. 10.1016/j.ijimpeng.2013.12.006
50. Shih Y-S, Chen J-J. The stress intensity factor study of an elliptical cracked shaft. Nuclear Engineering and design. 2002;214(1-2):137-45. 10.1016/S0029-5493(02)00022-5
51. Rice JR, Rosengren G. Plane strain deformation near a crack tip in a power-law hardening material. Journal of the Mechanics and Physics of Solids. 1968;16(1):1-12. 10.1016/0022-5096(68)90013-6
52. Dong P, Pan J. Elastic-plastic analysis of cracks in pressure-sensitive materials. International journal of solids and structures. 1991;28(9):1113-27. 10.1016/0020-7683(91)90106-P
53. Xia L, Wang T, Shih C. Higher-order analysis of crack tip fields in elastic power-law hardening materials. Journal of the Mechanics and Physics of Solids. 1993;41(4):665-87. 10.1016/0022-5096(93)90022-8
54. Nikishkov G, Matvienko YG. Elastic–plastic constraint parameter A for test specimens with thickness variation. Fatigue & Fracture of Engineering Materials & Structures. 2016;39(8):939-49. 10.1111/ffe.12390
55. El Arem S. On the mechanics of beams and shafts with cracks: A standard and generic approach. European Journal of Mechanics-A/Solids. 2021;85:104088. 10.1016/j.euromechsol.2020.104088
56. Liu Y, Glass G. Effects of mesh density on finite element analysis. SAE Technical Paper; 2013. Report No.: 0148-7191.
57. Bhalerao GN, Patil AA, Waghulde KB, Desai S. Dynamic analysis of rotor system with slant cracked shaft. Materials Today: Proceedings. 2021;44:4268-81. 10.1016/j.matpr.2020.10.544
58. Lap-Arparat P, Tuchinda K. Computational Study of Excitation Controlling Parameters Effect on Uniform Beam Deformation under Vibration. International Journal of Engineering, Transactions A: Basics. 2023;36(1):60-70. 10.5829/IJE.2023.36.01A.08
59. Carpinteri A. Shape change of surface cracks in round bars under cyclic axial loading. International Journal of Fatigue. 1993;15(1):21-6. 10.1016/0142-1123(93)90072-X
60. Miedlar PC, Berens AP, Gunderson A, Gallagher J. Analysis and support initiative for structural technology (ASIST) delivery

order 0016: USAF damage tolerant design handbook: guidelines for the analysis and design of damage tolerant aircraft structures. University of Dayton Research Institute: Dayton, OH, USA. 2002.

61. Shin C, Cai C. Experimental and finite element analyses on stress intensity factors of an elliptical surface crack in a circular shaft under tension and bending. International Journal of fracture. 2004;129:239-64. 10.1023/B:FRAC.0000047784.23236.7d
62. Astiz M. An incompatible singular elastic element for two-and three-dimensional crack problems. International Journal of Fracture. 1986;31:105-24. 10.1007/BF00018917
63. Couroneau N, Royer J. Simplified model for the fatigue growth analysis of surface cracks in round bars under mode I. International Journal of Fatigue. 1998;20(10):711-8. 10.1016/S0142-1123(98)00037-1
64. Wahrhaftig AdM, Magalhães KMM. Bifurcation Analysis of Columns of Composite Materials with Thermal Variation. Materials Research. 2021;24. 10.1590/1980-5373-MR-2021-0266

Persian Abstract

چکیده

مکانیسم‌های پشت تغییر شکل دما و مواد در ویبروترموگرافی همچنان مشکوک هستند و شکافی در درک ایجاد می‌کنند. این مطالعه مکانیسم ناشی از تغییر شکل را بررسی می‌کند و تنها بر تولید گرما مرتبط با توسعه کرنش تمرکز می‌کند. هر دو روش تجربی و شبیه سازی گنجانیده شده است. بخش تجربی رابطه دما–کرنش ماده SCM440 را که معمولاً برای شفت‌های چرخشی استفاده می‌شود، بررسی می‌کند. این رفتار از طریق ارتباط بین تغییر دما و تغییر شکل ماده در طول آزمایش کشش تک محوری بررسی می‌شود. نتایج نشان می دهد که تغییر دما و توزیع را می توان بر اساس توسعه کرنش پلاستیک پیش بینی کرد. شبیه‌سازی روش المان محدود (FEM) برای مدل‌سازی برانگیختگی شفت با و بدون ترک سطحی بیضوی استفاده می‌شود. پیکربندی‌های مختلف شفت ترک خورده بررسی می‌شوند و الگوهای تولید و توزیع کرنش متمایز را آشکار می‌کنند. تغییر کرنش بالا به طور قابل توجهی در اطراف نوک ترک مشاهده می شود که امکان تشخیص ناپیوستگی شفت را فراهم می کند. در نتیجه، یک تکنیک پیش‌بینی دما برای تخمین دما بر اساس تغییر کرنش در طول تغییر شکل توسعه داده می‌شود. قدرت تحریک کافی و استفاده از دوربین IR با حساسیت بالا برای کاربرد موثر تکنیک پیش‌بینی دما توصیه می‌شود. علاوه بر این، این مطالعه بینش‌هایی را در مورد درک کاربرد و محدودیت‌های لرزش‌گرموگرافی برای بازرسی آسیب اجزای مهندسی بر اساس روابط تجربی دما–کرنش و پیش‌بینی‌های محاسباتی توزیع کرنش در شفت‌های ترک خورده تحت تحریک ارائه می‌کند. این یافته‌ها راهنمایی برای کاربردهای مهندسی و تلاش‌های تحقیقاتی آینده ارائه می‌کنند.